



**HAL**  
open science

## **Sr immobilization in irradiated Portland cement paste exposed to carbonation**

Gabriela Bar-Nes, Ofra Klein-Bendavid, Laure Chomat, Nathalie Macé, Michal Arbel-Haddad, Stéphane Poyet

### ► **To cite this version:**

Gabriela Bar-Nes, Ofra Klein-Bendavid, Laure Chomat, Nathalie Macé, Michal Arbel-Haddad, et al.. Sr immobilization in irradiated Portland cement paste exposed to carbonation. *Cement and Concrete Research*, 2018, 107, pp.152 - 162. <10.1016/j.cemconres.2018.02.015>. <cea-03293668>

**HAL Id: cea-03293668**

**<https://cea.hal.science/cea-03293668v1>**

Submitted on 21 Jul 2021

**HAL** is a multi-disciplinary open access archive for the deposit and dissemination of scientific research documents, whether they are published or not. The documents may come from teaching and research institutions in France or abroad, or from public or private research centers.

L'archive ouverte pluridisciplinaire **HAL**, est destinée au dépôt et à la diffusion de documents scientifiques de niveau recherche, publiés ou non, émanant des établissements d'enseignement et de recherche français ou étrangers, des laboratoires publics ou privés.



HAL Authorization

# 1 **Sr immobilization in irradiated Portland cement paste exposed to carbonation**

2 **Gabriela Bar-Nes<sup>1\*</sup>, Ofra Klein-BenDavid<sup>1</sup>, Laure Chomat<sup>2</sup>, Nathalie Macé<sup>2</sup>, Michal Arbel-Haddad<sup>1</sup>,**  
3 **Stephane Poyet<sup>2</sup>**

4 <sup>1</sup> Department of Applied Chemistry, NRCN, P.O. Box 9001, Beer-Sheva, Israel.

5 <sup>2</sup> Den-Service d'Etude du Comportement des Radionucléides (SECR), CEA, Université Paris-Saclay, F-91191, Gif-sur-Yvette, France

6 \*Corresponding author: gabi.barnes@gmail.com

## 8 **Abstract**

9  
10 Cement based materials are widely used as binding matrices for radionuclides in low and  
11 intermediate level waste management applications. We studied the effect of irradiation and  
12 carbonation under atmospheric condition on the leaching of Sr from Portland cement paste.  
13 Samples were exposed to gamma irradiation or subjected to thermal treatment under either inert  
14 or atmospheric conditions. Leaching tests were performed and supplemented by post-leaching  
15 characterization including local chemical analysis (LA-ICPMS) crystallographic analysis (XRD),  
16 and EPMA imaging. The combination of these methods enabled us to link between the  
17 crystallography, texture and composition of the treated samples and their ability to retain Sr ions.  
18 Results show that carbonation was the main factor determining the retention of Sr ions, whereas  
19 irradiation did not have a significant effect. Moreover, carbonation has a positive effect on the  
20 retention of Sr ions in the matrix with the formation of a carbonated zone.

21

22 **Keywords:**

23 cement paste (D), carbonation (C), radioactive waste (E), leaching, characterization (B)

24

## 25 1. Introduction

26

27 Cement based materials are widely used in the nuclear industry for low and intermediate level  
28 waste management applications due to their availability, low cost, good chemical compatibility  
29 with waste ions and mechanical stability. The prediction of the long-term behavior of cementitious  
30 waste packages requires the identification and the understanding of degradation mechanisms that  
31 might affect the structure. One of these degradation mechanisms is water radiolysis, resulting from  
32 the immobilized radioactive waste elements, which leads to dehydration and release of H<sub>2</sub> gas, and  
33 thus carries potential impacts on the safety of the wasteform [1,2]. Cement carbonation occurring  
34 at atmospheric conditions (in presence of CO<sub>2</sub>), is an additional degradation mechanism that could  
35 affect the waste-form stability [2,3]. The temperature increase induced by the irradiation could  
36 produce favorable conditions for enhanced carbonation. The extent of carbonation depends on CO<sub>2</sub>  
37 partial pressure [4-6], moisture content in the sample pores [4,7-9] and temperature [10-12].  
38 Although the carbonation reaction occurs in the aqueous phase and therefore slows down as water  
39 activity decreases, at highly saturated conditions the diffusion of carbon dioxide is reduced and  
40 even inhibited by water filling the pores. Therefore, carbonation occurs most rapidly at  
41 intermediate saturation of the cement paste.

42 There are few published data on the effect of irradiation on the immobilization of radioactive waste  
43 in cement based materials. One of the studies [2] concluded that the enhanced carbonation  
44 associated with irradiation, leads to crystallographic, textural and chemical modifications and thus  
45 affects the immobilization of radionuclides in the matrix. The effect of carbonation on the leaching  
46 resistance of cementitious pastes has been extensively studied [13-16], but contradictory results  
47 were reported. These contradictions originate from the fact that in some cases carbonation might  
48 improve waste retention either by precipitation as insoluble carbonates, or due to the reduced

49 porosity of the carbonated matrix, while in other cases retention was reduced, possibly as a result  
50 of micro-cracking due to shrinkage during carbonation or rearrangement in pore connectivity [15-  
51 19].

52 The objective of this study is to gain understanding concerning the combined effect of irradiation  
53 and carbonation on Sr retention in cement paste. The experimental approach included the exposure  
54 of cement samples to different degradation mechanisms (irradiation and thermal treatment under  
55 either inert or atmospheric conditions) followed by leaching tests. The samples were studied using  
56 XRD, to obtain their crystalline phase composition before and after treatment and leaching. LA-  
57 ICP-MS and EPMA were applied to explore the local changes in the chemical composition due to  
58 the various treatments, allowing the evaluation of the different treatments on the durability and  
59 leaching resistivity of cementitious pastes.

## 60 2. Experimental

### 61 2.1. Sample preparation

62 The cement used for this study is a CEM I Val d'Azergues cement from Lafarge Company  
63 (France). It is composed of 96% of clinker, 1% of filler and 3% of gypsum. The chemical  
64 composition of the cement is presented in Table 1. Cementitious samples were prepared with a  
65 water to cement ratio (w/c) of 0.4. A non-radioactive Sr solution, using the nitrate salt,  $\text{Sr}(\text{NO}_3)_2$   
66 (Aldrich chemicals), has been added to the cement to prepare a Sr-spiked-cementitious paste, in  
67 order to simulate a waste stream to be cemented, with a target Sr concentration of 3.66 mg Sr/g  
68 paste. Non-spiked (blank) samples were prepared in order to assess the effect of the Sr addition on  
69 the on the crystallography, texture and composition of the paste.

70 All specimens were cast in plastic molds (diameter of 40 mm and height of 100 mm) and sealed.  
71 After setting, the samples were de-molded, inserted into polypropylene bags, sealed again and  
72 allowed to self-cure at room temperature for 28 days. The cured specimens were sliced using a  
73 diamond saw into 15 mm thick disc shaped samples. The list of samples is presented in Table 2.

## 74 2.2 Degradation procedures

### 75 2.2.1 Gamma irradiation

76 Sample irradiation was performed using a  $^{60}\text{Co}$  source in a commercial irradiation facility (Sorvan  
77 Ltd, Israel). The irradiation has been performed at a dose rate of 24 Gy/min, over a period of 6  
78 months, to reach a total dose of  $5.0 \times 10^6$  Gy.

79 Samples were irradiated either under inert conditions or exposed to the ambient atmospheric  
80 conditions of the irradiation cell. Samples irradiated under inert conditions were placed in Pyrex®  
81 ampoules and sealed at sub-atmospheric pressure (500 torr) and under an Ar atmosphere. As the  
82 irradiation cell lacks climate control, fluctuations in the atmospheric conditions are expected  
83 during the irradiation period. The average operating temperature and the relative humidity in the  
84 irradiation chamber were  $\sim 40^\circ\text{C}$  and  $\sim 30\%$ , respectively.

### 85 2.2.2 Thermal degradation

86  
87 Samples exposed to thermal degradation were polished before the treatment in order to remove  
88 any possible surface alteration prior to the experiment.

89 Samples were placed inside a climatic chamber at 40°C, 32% RH at atmospheric conditions for 6  
90 months. Samples treated under inert conditions were placed in a reactor filled with N<sub>2</sub> at 32% RH,  
91 fixed by a MgCl<sub>2</sub> saturated solution [20], inside the same climatic chamber.

## 92 2.3 Characterization methods

### 93 2.3.1 XRD analysis

94

95 Crystallographic characterization was performed using X-Ray diffraction (XRD). Measurements  
96 were carried out using a PANalytical X'Pert diffractometer (Cu K $\alpha$ ,  $\lambda = 1.54 \text{ \AA}$ ), on the angular  
97 range of 5° - 65°, in increments of 0.017° or 0.033°.

98 XRD analyses were performed on bulk samples. Analysis of bulk samples eliminates a preliminary  
99 grinding and avoids possible effects of preferential orientation encountered in the powder method.

100 In order to obtain XRD profiles, the polished surface was analyzed, consequently a thin layer of  
101 the sample (from 30 to 150  $\mu\text{m}$  of thickness) was removed by polishing and the newly exposed  
102 surface was then analyzed. This method allowed us to obtain a series of diffractograms as a  
103 function of the depth of the sample. Prior to the XRD characterization, five points were marked on  
104 the bottom of the sample and the sample thickness at each of the points was measured using a  
105 micrometer screw gauge. The samples were then manually polished using 120 grit silicon carbide  
106 paper. After each polishing step, the sample thickness was measured again at each of the 5 points  
107 using the micrometer screw gauge. For each of the 5 measured points the difference between the  
108 initial thickness and the measured thickness (which refers to the measured depth) was calculated.  
109 The average of all 5 points was denoted as the sample depth analysed. Grinding was performed up

110 to a depth of approximately 3500  $\mu\text{m}$  in the sample, until reaching the non-altered part of the  
111 sample.

112 XRD results were analyzed using the Reference Intensity Ratio (RIR) method [21](Johnson and  
113 Zhou, 2000) which scales all diffraction data to a Corundum ( $\text{Al}_2\text{O}_3$ ) standard. The RIR factors  
114 were obtained from ICSD using POWD-12++ and are presented in Table 3. The scale factors are  
115 determined from the strongest intensity lines of both the analyte and corundum. In cases where the  
116 calculation was performed using a different diffraction line, an additional correction factor was  
117 applied, proportional to the relative intensity of the chosen diffraction line as compared to the  
118 strongest diffraction line, denoted here as peak fraction.

119 Due to the presence of non-crystalline phases in the cementitious matrix, the RIR approach was  
120 used as a semi-quantitative method, allowing us to normalize the diffraction intensities, and thus  
121 making qualitative comparison only between the different crystalline phases in a specific sample.  
122 Therefore the results are presented as intensity normalized by RIR factor and the peak fraction  
123 (Table 3).

### 124 2.3.2 LA-ICPMS analysis

125 Cement samples were cleaved, exposing a cross-section extending from the surface into the sample  
126 core. Each sample was placed in a cell equipped with an inlet nozzle of 0.5 mm diameter. Laser  
127 ablation was conducted using an ArF-excimer laser (New Wave) emitting 15 ns long pulses at a  
128 wavelength of 193 nm, with repetition rate of 10 Hz, at a power of 7  $\text{J}/\text{cm}^2$ , with fluence of 5.05  
129  $\text{J}/\text{cm}^2$ . The cell was flushed with 0.5 L/min helium, washing the vaporized sample into the mass  
130 spectrometer. SRM NIST610 glass was used as standard. Ablation of the standard was conducted  
131 at the beginning and the end of each ablation session, at a spot size of 50  $\mu\text{m}$ .

132 The analyzed spot size varied across the cement samples in order to attain maximal resolution near  
133 the surface where leaching and precipitation are expected to have the strongest effect, and a lower  
134 resolution but higher signal at inner sample areas. A spot size of 10  $\mu\text{m}$  was used at the outermost  
135 120  $\mu\text{m}$  of the sample, then a spot size of 50  $\mu\text{m}$  was applied for the next 900  $\mu\text{m}$ , and finally a  
136 spot size of 100  $\mu\text{m}$  was used for the innermost 3000-4000  $\mu\text{m}$ .

137 The ICP-MS analysis was conducted by AGILENT (7500 CX) ORS quadrupole mass  
138 spectrometer with a RF power of 1500W, injection tube diameter of 2.0 mm, nebulizer and  
139 auxiliary gas flows of 0.9 L/min Ar .

140 Table 4 lists the analyzed isotopes, the average limit of detection for the different isotopes at  
141 different spot sizes and the average analytical error for the various isotopes as a function of the  
142 spot size used.

143 For all three spot sizes the average error is generally lower than 3% (except for Ba in the 10  $\mu\text{m}$   
144 spot size) An average error lower than 1% is obtained for all isotopes at 100  $\mu\text{m}$  spot size. For  
145  $^{88}\text{Sr}$  and  $^{42}\text{Ca}$ , the most important analytes in this paper, the analytical error is  $\leq 1\%$ .

146  $\text{SiO}_2$  was used as an internal standard, at a concentration of 20.6% (the concentration measured in  
147 the original cement powder).

148  $\text{SiO}_2$  was used as its concentration is relatively high, thus, it is easily detected using the ICP-MS.

149 Furthermore, Si concentration is not expected to decrease significantly due to leaching effects.

150 In order to obtain coherent concentration display between all the samples, the different element  
151 concentrations (C) are presented relative to the concentration of the innermost spot analyzed (C0),  
152 assuming that this point resides within the undisturbed inner sample volume.

153 Figure 1 shows the normalized  $^{25}\text{Mg}$  and  $^{42}\text{Ca}$  signals obtained as a function of distance from the  
154 surface of a leached sample, together with the analyzed spot size used. These results demonstrate

155 that in spite of the higher limit of detection and larger error for the smaller spot size, spot size has  
156 no effect on the calculated concentration of Mg, representing an element with minimal leaching.  
157 Additionally, no correlation was found between the spot size used and the concentration calculated  
158 for Ca, confirming that concentration changes are not an artifact of the spot size.

159

### 160 2.3.3. EPMA (Electron Probe Micro-Analysis)

161

162 Samples were impregnated in epoxy (Epofix by Struers) using a Citovac device (by Struers) for  
163 10 min at a pressure of 0.73 bar. The impregnated samples were polished parallel to the sample  
164 surface using a Saphir 250 polishing machine manufactured by ATM. The samples were initially  
165 polished using SiC polishing paper with 320, 600 and 1200 grid, and finally using a diamond  
166 suspension of 3 and 1  $\mu\text{m}$ . Samples were then carbon coated and mounted on the EPMA stand.  
167 EPMA imaging and analyses were conducted using a JEOL 8230 superprobe EPMA with EDS  
168 (Energy-Dispersive X-ray Spectroscopy) and four wavelength-dispersive spectrometers (WDS)  
169 for microanalysis. Beam conditions were set to 15 keV and 15 nA. Silicate and oxide standards  
170 were used for EDS analyses. Data was processed with a PRZ correction procedure. Back-scattered  
171 electron (BSE) and secondary (SEC) electron imaging were applied.

### 172 2.4 Leaching experiments

173 The leaching tests were performed according to the standard ANS-16.1 procedure [22], using  
174 deionized water as the leachant. According to this procedure, the leachant volume ( $\text{cm}^3$ ) equals 10  
175 times the surface area of the tested sample ( $\text{cm}^2$ ). Samples were immersed for 90 days, with  
176 leachant replacement at predetermined leaching intervals of 2, 7, 24, 48, 72, 96, 120, 456, 1128,

177 and 2136 hours. Following the standard procedure, the leaching tests were performed in closed  
178 vessels under static, atmospheric conditions.

179 Leaching tests have been performed for samples treated under the different conditions and for  
180 untreated reference samples. Duplicate samples containing Sr were tested except for the sample  
181 irradiated at inert conditions, for which a single sample was available.

182 To assess the effect of initial Sr concentration on the leachability, an additional blank sample  
183 prepared with no Sr doping was tested.

184 The concentrations of Sr and Ca in the leachate were determined using Inductive Coupled Plasma  
185 Optical Emission Spectroscopy (SPECTRO ARCOS ICP-OES) for each leaching interval.

### 186 3. Results

#### 187 3.1 Crystallographic characterization of untreated HPC (hydrated Portland cement) samples

188 The powder diffraction pattern of a crushed non-treated sample (not presented) displays the typical  
189 crystallographic composition for a CEM I cementitious paste: portlandite ( $\text{Ca}(\text{OH})_2$ ), ettringite  
190 ( $\text{Ca}_6\text{Al}_2(\text{SO}_4)_3(\text{OH})_{12}\cdot 26\text{H}_2\text{O}$ ) and C-S-H (calcium silicate hydrate phases) as hydrated phases and  
191 possible presence of a small amount of calcite ( $\text{CaCO}_3$ ) and some residual anhydrous phases ( $\text{C}_4\text{AF}$   
192 for  $(\text{CaO})_4\text{Al}_2\text{O}_3\text{Fe}_2\text{O}_3$ ,  $\text{C}_2\text{S}$  for  $(\text{CaO})_2\text{SiO}_2$  and  $\text{C}_3\text{S}$  for  $(\text{CaO})_3\text{SiO}_2$ ). As expected, no Sr bearing  
193 phases have been identified by XRD analysis.

## 194 3.2 Characterization of treated HPC samples

### 195 3.2.1 Characterization of samples aged under inert conditions

196 Surface XRD analysis of samples treated under inert conditions (not presented) showed the full  
197 disappearance of ettringite. Additionally, in the irradiated samples calcite was detected at the  
198 surface, with a corresponding depletion of portlandite. This superficial precipitation had probably  
199 occurred during sample preparation. Calcite was not found at the surface of the sample treated in  
200 the climatic chamber which was polished prior to the thermal treatment (section 2.2.2).

201 EPMA imaging of a sample irradiated under inert conditions and the corresponding relative  
202 concentrations of Ca, Ba and Sr as obtained by LA-ICPMS are presented in Figures 2 and 3,  
203 respectively. The EPMA BSE image of the sample shows a very thin uneven front (10-100  $\mu\text{m}$ ) at  
204 the sample surface, with a denser but brighter appearance (Fig. 2), while the rest of the sample  
205 remains virtually unchanged.

206 The concentration profiles of Sr, Ca, and Ba along a cross-section in the same sample (Fig. 3)  
207 indicate a constant concentration for these three elements throughout most of the sample, except  
208 for the 80-100  $\mu\text{m}$  outer surface, where the concentration of all three elements shows significant  
209 scatter. This scatter might reflect the uneven precipitation of a carbonate phases near the surface.

210 The precipitation of such phases is probably due to exposure to atmospheric conditions during  
211 sample preparation. These results are in agreement with the formation of a thin calcite layer at the  
212 sample surface as observed by XRD, and with the EPMA-BSE image showing a thin dense layer  
213 at the sample surface.

214

### 215 3.2.2 Characterization of samples treated under atmospheric conditions

216 Samples aged under atmospheric conditions, either in the climatic chamber or during the  
217 irradiation process, present similar crystallographic patterns.

218 The crystallographic composition of both samples consists of calcite near the surface of the sample  
219 with corresponding disappearance of the portlandite. Further into the sample aragonite and  
220 vaterite, the two metastable calcium carbonate phases, occur. The formation and stability of these  
221 two phases are favored over calcite at temperatures above 40°C [23,24]. The overall thickness of  
222 the carbonated zone, defined by the presence of calcium carbonate phases, is about 3500  $\mu\text{m}$ , for  
223 both irradiated and non-irradiated samples (Fig. 4).

224 Samples treated in the climatic chamber exhibited cracking after three days of treatment (Fig. 5),  
225 probably due to the enhanced drying process.

### 226 3.3 Leaching results

227 Leaching experiments were performed for samples exposed to various aging treatments as well as  
228 for untreated reference samples. Figures 6 and 7 present the average cumulative fraction of Sr and  
229 Ca ions leached for the different samples *vs.* square root of time.

230 The overall cumulative fraction values obtained for Sr were higher than for Ca, although the trends  
231 were similar. For the reference sample, for example, the cumulative fraction of Sr was five times  
232 higher than for Ca (0.09 and 0.018 respectively).

233 For samples aged under atmospheric conditions, and hence exposed to carbonation, the cumulative  
234 fraction of both Sr and Ca ions leached was lower than for untreated reference samples, with no  
235 apparent difference between the irradiated and climatic chamber samples.

236 The sample that has been exposed to irradiation under inert atmosphere showed a slight increase  
237 in the cumulative Sr and Ca leached fraction compared with the reference sample. Significant  
238 increase in the leached fraction of Sr and Ca was obtained for the samples that were treated in the  
239 climatic chamber under inert atmosphere. For these samples the Sr and Ca cumulative fractions  
240 increased from values of 0.09 and 0.018 in the reference sample, to values of 0.35 and 0.044;  
241 respectively.

242 The difference between the results obtained for irradiated and climatic chamber samples treated  
243 under inert atmosphere could be a result of differences in the sample pre-treatment. As presented  
244 in section 3.2.1, the irradiated sample showed a thin carbonation zone. Such carbonation zone was  
245 not found for the samples treated in the climatic chamber, which were polished before treatment.

246 The effect of initial Sr concentration on the Sr retention can be studied from the leaching curves  
247 of the two samples irradiated under inert conditions (Fig. 8), one doped with Sr and the other  
248 containing the native Sr content from CEM I cement (3660 ppm vs. 250 ppm respectively).  
249 Despite the large difference in the initial Sr concentration the cumulative leached fractions  
250 obtained were almost similar. Similar leachabilities were observed for both samples during the  
251 early stages of leaching, while a slightly higher leached fraction for the sample doped with Sr was  
252 measured at the later stages of the experiment.

### 253 3.4 Post leaching characterization

254 The distribution of the alkaline earth elements Sr, Ba and Ca within the leached samples, as  
255 obtained from LA-ICP-MS, will be presented together with the phase distribution as obtained from  
256 XRD depth profile measurements and complemented with EPMA images. Sr was considered as  
257 waste simulant, while Ca is a major cement component and Ba is a trace element present in cement.

258 Both Sr and Ba may substitute Ca in various mineral phases (especially carbonates) with high  
259 compatibility [25].

### 260 3.4.1 Post-leaching characterization of untreated reference sample

261 The untreated sample that served as a reference for the leaching test was analyzed after leaching.  
262 Figure 9 presents the EPMA BSE image of the sample. A very distinct disturbed zone can be  
263 detected at the surface. This zone, which is composed of several sub-zones, has an overall thickness  
264 of 700  $\mu\text{m}$ .

265 The Sr, Ca and Ba relative concentration profiles along this reference sample are presented in  
266 Figure 10. All three elements show a decrease in relative concentration moving from the inner  
267 undisturbed zone ( $C/C_0 = 1$ ) towards the surface of the sample.

268 For all three elements, the concentration is relatively constant along the outer 700  $\mu\text{m}$ , except for  
269 the outermost  $\sim 150$   $\mu\text{m}$ , where a large dispersion of the concentrations was found. This region  
270 roughly corresponds to the disturbed zone in figure 9. Further into the sample a relatively constant  
271 increase in the Sr concentration, with no corresponding morphological changes in the BSE image,  
272 is obtained until  $\sim 1600$   $\mu\text{m}$ , where the concentration levels to  $C/C_0 = 0.8$ . A further increase in the  
273  $C/C_0$  is observed at  $\sim 3000$   $\mu\text{m}$  reaching the level of  $C/C_0 = 1$  at  $\sim 4000$   $\mu\text{m}$ . For both Ca and Ba the  
274 concentration reaches the level of  $C/C_0 = 1$  at  $\sim 1000$   $\mu\text{m}$ .

275 Figure 11 presents the XRD profile of the same sample. At the surface, a carbonated zone is  
276 detected, indicated by the presence of calcite together with a reduction in the portlandite intensity.  
277 The normalized intensity for calcite is relatively high for the first 300  $\mu\text{m}$  from the surface of the  
278 sample and then is gradually decreases up to a depth of approximately 800  $\mu\text{m}$  into the sample,  
279 roughly corresponding to the disturbed depth as observed by EPMA (Fig. 9) and to the constant  
280 concentrations of all three elements studied (Fig. 10).

### 281 3.4.2 Post-leaching characterization of samples aged under inert conditions

282 Figure 12 presents an EPMA BSE image of the sample treated in the climatic chamber under inert  
283 conditions. The image presents a highly porous, irregular dark area at the sample surface and along  
284 two deep cracks which are perpendicular to the surface. These cracks seem to be inter-connected  
285 and penetrate approximately 1000  $\mu\text{m}$  into the sample. The bulk of the sample contains a brighter,  
286 denser looking material.

287 Figure 13 presents the element concentrations along a cross-section of the samples aged under  
288 inert conditions. Both samples show relatively large scatter of all three elements within the 100  
289  $\mu\text{m}$  nearest to the surface, followed by a relatively constant concentration of all three elements up  
290 to a depth of 500-700  $\mu\text{m}$ .

291 Further into the sample, the Sr concentration gradually increases until reaching values similar to  
292 those of the undisturbed region ( $C/C_0 = 1$ ) at a depth of about 3000  $\mu\text{m}$  for the irradiated sample  
293 and 3800  $\mu\text{m}$  for the sample treated in the climatic chamber. The Ca and Ba concentration profiles  
294 show a step-like increase at a depth of 700  $\mu\text{m}$ , reaching a constant value of  $\sim C/C_0 = 1$ .

295 XRD measurements of the above samples reveal the depletion of portlandite from the outermost  
296 region. Portlandite is detected at a depth of approximately 500-700  $\mu\text{m}$  from the surface, in  
297 accordance with the Ca concentration profile. Both samples show the presence of calcite at the  
298 sample surface, gradually decreasing to a depth of approximately 500-700  $\mu\text{m}$  (Fig. 14). Higher  
299 intensity values of calcite were measured for the irradiated sample, in accordance with the higher  
300 scatter at the surface probably due to an initial carbonation layer present in the sample, as  
301 previously discussed in sections 3.2.1 and 3.3.

### 302 3.4.3 Post-leaching characterization of samples treated under atmospheric conditions

303 Figure 15 presents an EPMA BSE image of the sample treated in the climatic chamber under  
304 atmospheric conditions. A thin (50-80  $\mu\text{m}$ ) porous rim is observed at the outer surface of the  
305 sample. Porous regions are also observed along cracks which are perpendicular to the surface and  
306 penetrate up to 300  $\mu\text{m}$ . Beyond this porous rim, a zone of denser and brighter material, having a  
307 thickness of 200  $\mu\text{m}$ , is observed. The inner part of the sample keeps a relatively uniform  
308 appearance.

309 Figure 16 presents the Ca, Sr and Ba relative concentration cross section along two samples  
310 exposed to atmospheric conditions, either irradiated or treated in the climatic chamber. Both  
311 samples show significant scatter near the surface. For the sample treated in the climatic chamber,  
312 all three elements are depleted in the outermost 100  $\mu\text{m}$ . For the irradiated sample Sr and Ba are  
313 enriched in the outermost 100  $\mu\text{m}$ . The concentration of all three elements was found to increase  
314 from a depth of  $\sim 100$  to  $\sim 1000$   $\mu\text{m}$ . The Ca concentration reaches its undisturbed concentration  
315 ( $C/C_0 \sim 1$ ) at  $\sim 1000$   $\mu\text{m}$  into the sample. For Sr and Ba, however, enrichment relative to the initial  
316 concentration ( $C/C_0 > 1$ ) is observed at a depth range of 700-4000  $\mu\text{m}$ , with a gradual decrease back  
317 to the undisturbed value.

318 Figure 17 presents the XRD measurements of the above samples. In both cases portlandite is  
319 depleted from the surface up to a depth of 250-300  $\mu\text{m}$ . From this depth inward there is a gradual  
320 increase in portlandite to its maximal intensity.

321 Calcite was found at the surface of both samples. Its intensity decreases towards the inner part of  
322 the sample and levels off at around 300  $\mu\text{m}$  depth. The vaterite and aragonite phases are present  
323 up to 3500  $\mu\text{m}$  from the surface. The intensity curves slightly differ between the two samples.  
324 While for the sample treated in the climatic chamber maximal intensity for both phases was  
325 detected at around 50-100  $\mu\text{m}$  from the surface, for the irradiated sample both carbonate phases

326 were not detected at the surface and appeared at a depth of 100  $\mu\text{m}$  with a maximal intensity around  
327 150  $\mu\text{m}$ . For both samples the normalized intensity of vaterite was higher than that of aragonite.

#### 328 4. Discussion

##### 329 4.1 Leaching effect – samples treated under inert conditions

330 The post-leaching reactive concentration profiles obtained for samples aged under inert  
331 atmosphere, present an extended disturbed profile for all three examined elements, as compared to  
332 the reference sample. This corresponds well with the higher cumulative leached fraction obtained  
333 for these samples, possibly due to the formation of microcracks, which is known to occur during  
334 the enhanced drying process.

335 When comparing the two samples treated under inert conditions, it can be seen that the sample  
336 treated in the climatic chamber shows much higher leachability and deeper depletion profile  
337 relative to the sample exposed to irradiation.

338 As already discussed in section 3.2.1, the major difference between these two samples was the  
339 very thin carbonated layer present in the irradiated sample which was prior to treatment removed  
340 by polishing from the sample placed in the climatic chamber. This carbonated layer, a few tens of  
341 micrometers thick, may contribute to the reduced leachability of the sample irradiated under inert  
342 atmosphere.

343 An additional reason for the difference between the two samples could be the increased  
344 dehydration and consequent cracking due to the lower RH conditions (32%) fixed in the climatic  
345 chamber, compared to the irradiated sample sealed in an ampoule and thus exposed to much higher  
346 relative humidity (>80%).

347 The cumulative leaching fractions of samples with different initial Sr concentration (3660 ppm vs.  
348 250 ppm Sr) were almost similar. A slightly higher leached fraction for the sample doped with Sr,  
349 may result from a higher fraction of Sr residing in the interstitial pores for the doped sample  
350 relative to the non-doped one, where a higher fraction of Sr is probably bound within the lattice  
351 sites.

352

#### 353 4.2 Leaching effect – samples treated under atmospheric conditions

354 In the present study samples were exposed to carbonation at 40°C either in a climatic chamber or  
355 during the irradiation process. Both samples exhibit a ~3500 µm thick carbonated layer, composed  
356 mainly of metastable calcium carbonate phases (vaterite and aragonite). The dominance of vaterite  
357 and aragonite in the carbonated layer is in agreement with previous studies showing that hexagonal  
358 vaterite precipitation predominates at 40°C, a temperature at which orthorhombic aragonite starts  
359 to form as well [26]. It was further shown that a high Sr concentration enhances aragonite  
360 precipitation [24,27]. Additionally Roncal-Herrero *et al.* [28] have shown that in the presence of  
361 Sr, vaterite can become the dominant carbonate phase even at relatively low temperatures (25°C)

362 .

363 The ~3500 µm thick carbonated front leads to the reduced leachability of the Sr ions, compared to  
364 the untreated sample. One possible mechanism for the reduction in ion leachability is porosity  
365 clogging which is characteristic to carbonated samples [29,30] as indicated by the densification of  
366 the carbonated zone observed in this study (Fig 15). Furthermore, it was shown that vaterite, which  
367 was found here as the dominant carbonate phase for these samples, has the lowest density among  
368 these carbonate polymorphs, and therefore could lead to increased pore clogging [31].

369 An additional process that can lead to reduced leachability of Sr is the co-precipitation of Sr into  
370 carbonate phases. Aragonite and vaterite have high coordination lattice sites for Sr and Ba and can  
371 easily accommodate these larger ions [24,32]. The measured partition coefficient values for Sr in  
372 aragonite is of the order of 1.1 at 40°C [33].

373 The effect of Sr co-precipitation in the metastable carbonate phases can be demonstrated by  
374 comparing Ca/Sr weight ratios in the cement paste and in the leachate solutions. In the original  
375 cement paste the Ca/Sr ratio is approximately 120. However, a much lower value of 30 was  
376 obtained for this ratio in the leachate of the reference sample, due to the preferential incorporation  
377 of Ca into crystalline phases and the C-S-H phase, whereas the Sr remains largely interstitial and  
378 more available to leaching. In the leachate of the carbonated samples the Ca/Sr ratio is ~45,  
379 indicating preferred Sr retention compared to the non-carbonated reference sample. This  
380 emphasizes the effect of Sr co-precipitation in aragonite and vaterite, increasing the Sr retention  
381 in the paste and thus reducing its relative leachability.

382 Therefore we may conclude that the clogging effect, which is expected to affect equally all ion  
383 mobilities and not to change the Ca/Sr ratio, is secondary in this case.

384 Additional evidence to the increased Sr retention induced by co-precipitation in aragonite and  
385 vaterite phases can be observed by the analysis of the solid matrix. The  $[Sr]/[Sr]_0$  ratio within an  
386 unleached sample is ~1 throughout the sample, with the exception of the outer surface zone where  
387 a large scatter in the results was detected (see section 4.4). All the leached samples that were treated  
388 under inert conditions as well as the reference sample show a decrease in the  $[Sr]/[Sr]_0$  ratio from  
389 a value of 1 in the undisturbed zone to a lower value towards the surface. However, in the samples  
390 treated under atmospheric conditions a local enrichment in the  $[Sr]/[Sr]_0$  ratio is measured within  
391 the aragonite/vaterite precipitation zone, where this ratio reaches the range of 1.2 - 1.4 (Fig. 16).

392 The relative enrichment of Ba in the carbonated front may be related to a similar process occurring  
393 due to preferred Ba precipitation in aragonite [34].

394 It is suggested that this enrichment has occurred during the initial carbonation process.  
395 Vaterite/aragonite precipitation during the treatment has reduced the local Sr concentration in the  
396 pore solution, creating a local gradient in Sr concentration and thus yielding a driving force for Sr  
397 diffusion from the surrounding areas to the carbonate precipitation zone. Continuous precipitation  
398 of Sr and Ba caused the observed relative enrichments, and thus increased the Sr and Ba ions  
399 retention within the sample.

400 It is interesting to note that although the sample carbonated in the climatic chamber showed  
401 evidence of cracking at an early stage of the treatment (Fig. 5), this cracking did not lead to higher  
402 Sr leachability, supporting the suggestion that Sr immobilization is dominated by its enhanced co-  
403 precipitation in the carbonated layer.

#### 404 4.3 The calcite surface layer effect

405 In the analyzed unleached sample, the relative concentration of Ca, Sr and Ba at the outer surface  
406 layer showed a large scatter with values ranging between 0.6 and 1.4 (Fig. 3). We suggest that this  
407 phenomenon is related to calcite precipitation during sample handling at atmospheric conditions,  
408 creating a very thin (10-100  $\mu\text{m}$ ) carbonated layer.

409 Additionally, in all leached samples, either treated or untreated, a calcite layer was detected at the  
410 outer surface of the sample with thickness varying between 100-500  $\mu\text{m}$ .

411 Calcite precipitation during leaching is reflected in the leaching curves where a change in the slope  
412 develops over the square root of time (Figures 6 & 7). A steeper slope was measured over the first  
413 7 days of leaching, whereas a more moderate slope persists over the remaining leaching process.

414 This effect was clearly demonstrated for the samples treated in the climatic chamber which have  
415 been polished before treatment and therefore they were lacking the initial calcite layer, making the  
416 effect more pronounced. This behavior is typical to the formation of a dense impervious  
417 carbonation layer and is consistent with previous results by Andac and Glasser [31]. Various other  
418 studies investigating the leaching of Portland cement pastes by hydrogeno-carbonate solutions  
419 [35,36] or natural waters containing CO<sub>2</sub> [37,38] have shown the formation of a calcite crust, at or  
420 near the paste–leachant interface, which strongly slows down the degradation process.

421 Within the near surface calcite layer significant scatter of the Ca, Sr and Ba concentrations occurs.  
422 When observing the chemical composition of this layer in leached samples under all treatments,  
423 Ca and Sr usually show a reduction in their relative concentration, whereas Ba shows a significant  
424 increase in its relative concentration (Figures 10,13&16)

425 The reason for this different behavior is related to the two simultaneous processes of leaching and  
426 calcite precipitation. Ca, as a major element, is effectively leached from the sample. Due to its  
427 high concentration in the matrix, the small amount of calcite precipitated does not affect the overall  
428 trend of the reduction in the Ca relative concentration.

429 On the other hand, Ba, being a trace element is significantly affected from minor precipitation  
430 processes. The relatively high Ba enrichment with respect to Sr is mainly the outcome of its lower  
431 concentration in the paste and hence higher sensitivity to precipitation processes. This  
432 phenomenon is widely used in geological studies, where trace elements are used to emphasize the  
433 precipitation of crystalline phases [39].

434 Moreover, the magnitude of this scatter for all three elements is much smaller for the samples  
435 treated in the climatic chamber (Fig. 13a) compared with the irradiated samples (Fig. 13b). This is

436 probably the consequence of the presence of the pre-leaching calcite layer in the later increasing  
437 the relative amount of calcite in the sample surface and therefore leading to higher scatter in the  
438 element concentrations.

## 439 5. Conclusions

440 The use of local chemical analysis (LA-ICP-MS) together with crystallographic analysis (XRD),  
441 supplemented by EPMA imaging, enabled us to link between the crystallography, texture and the  
442 composition of the treated samples and their ability to retain Sr ions in the system.

443 The cementation process is used for the conditioning of low and intermediate level radioactive  
444 waste; hence, the effects of irradiation and carbonation are intrinsic to the assessment of the  
445 process. However, in the present study no evidence of enhanced degradation mechanisms due to  
446 irradiation was found. Carbonation on the other hand, had shown a positive effect on the retention  
447 of Sr ions in the matrix with the formation of a distinct carbonated zone at the surface.

448 In the present study carbonation occurred in three different manners. 1) A very thin (up to 100  $\mu\text{m}$ )  
449 carbonated zone was formed during sample preparation and handling. This thin calcite layer was  
450 removed for the samples treated in the climatic chamber, leading to an increased Sr leachability  
451 compared to samples which were not polished before treatment. 2) All samples exhibited some  
452 carbonation (100-500  $\mu\text{m}$ ) during the leaching test, performed according to the ANSI-16.1  
453 procedure with no precaution taken to avoid exposure to the atmosphere. 3) For all samples  
454 exposed to enhanced carbonation at 40°C, a 3500  $\mu\text{m}$  thick carbonated layer, composed of  
455 metastable calcium carbonates (aragonite and vaterite) was formed. These carbonate phases

456 possess high coordination lattice sites for Sr (and Ba) and therefore can easily accommodate these  
457 larger ions [32,24].

458 The crystallographic and chemical composition of the samples as well as the retention of Sr ions  
459 (representing the immobilized waste) was highly influenced by the latter carbonation process. The  
460 extent of carbonation, as well as the crystallography and the Sr retention were similar for both  
461 carbonated samples with no additional effect found for the irradiated sample. Thus, carbonation  
462 enhanced by temperature increase, is sufficient to explain the retention behavior of strontium under  
463 the present atmospheric conditions. The correlation found between relative Sr enrichment and the  
464 presence of Ca-carbonate phases, clearly leads to the conclusion that during the carbonation  
465 treatment Sr ions are preferentially fractionated into these metastable carbonate phases, leading to  
466 a higher retention in the cement paste.

#### 467 References

468 [1] C. Gallé, H. Peycelon, P. Le Bescop, S. Bejaoui, V. L'Hostis, B. Bary, P. Bouniol, C. Richet,  
469 Concrete long term behavior in the context of nuclear waste management: Experimental and  
470 modeling research strategy, *Journal of Physics IV – Proceedings*. 136 (2006) 25-38.

471 [2] G. Bar-Nes, A. Katz, Y. Peled, Y. Zeiri, The combined effect of radiation and carbonation on  
472 the immobilization of Sr and Cs ions in cementitious pastes, *Materials and Structures* 41, (2008)  
473 1563-1570.

474 [3] F. Vodák, V. Vydra, K. Trtik, O. Kapickova, Effect of gamma irradiation on properties of  
475 hardened cement paste, *Materials and Structures*. 44 (2011) 101-107.

- 476 [4] V.G. Papadakis, C.G. Vayenas, M.G. Fardis, Fundamental modeling and experimental  
477 investigation of concrete carbonation, *ACI Materials Journal*. 88(4) (1991) 363-373.
- 478 [5] H. Hyvert, A. Sellier, F. Duprat, P. Rougeau, P. Francisco, Dependency of C–S–H  
479 carbonation rate on CO<sub>2</sub> pressure to explain transition from accelerated tests to natural  
480 carbonation, *Cement and Concrete Research*. 40, (2010) 1582-1589.
- 481 [6] M. Castellote, L. Fernandez, C. Andrade, C. Alonso C., Chemical changes and phase analysis  
482 of OPC pastes carbonated at different CO<sub>2</sub> concentrations, *Materials and Structures*. 42 (2009)  
483 515-525.
- 484 [7] G.J. Verbeck 1958 Carbonation of hydrated Portland cement, *Am Soc Test Mater*. 205,  
485 (1958) 17-36.
- 486 [8] H. Wierig, Longtime studies on the carbonation of concrete under normal outdoor exposure,  
487 *Proc. of RILEM seminar on the durability of concrete structures under normal outdoor exposure*,  
488 Hannover, Germany, (1984) 239-249.
- 489 [9] I. Galan, C. Andrade, M. Castellote, Natural and accelerated CO<sub>2</sub> binding kinetics in cement  
490 paste at different relative humidities, *Cement and Concrete Research*. 49 (2013) 21-28.
- 491 [10] Mori et al. 1972 On carbonation of Portland blast-furnace slag cement concrete,  
492 *Proceedings of the 26th general meeting of the Cement Association of Japan*, Tokyo, 184-188.
- 493 [11] T. Uomoto, Y. Takada, Factors affecting concrete carbonation ratio, *Concrete Library of*  
494 *JSCE* 21, (1993) 31-44.

495 [12] E. Drouet, S. Poyet, P. Le Bescop, J.M. Torrenti, J M, Chemical changes and carbonation  
496 profiles of carbonated cement pastes at 80°C for different relative humidities, Proceedings of  
497 CONSEC'10, 2010, Merida, Mexico.

498 [13] A.C. Garrabrants, F. Sanchez, D.S. Kosson, Changes in constituent equilibrium leaching  
499 and pore water characteristics of a Portland cement mortar as a result of carbonation, Waste  
500 Management, 24(1) (2004) 19–36.

501 [14] J.C. Walton, M.S. Bin Shafique, R.W. Smith, N. Gutierrez, A.J. Tarquin, Role of  
502 carbonation in transient leaching of cementitious wastefoms, Environmental Science and  
503 Technology. 31 (1997) 2345-2349.

504 [15] T. Van Gerven, D. Van Baelen, V. Dutre, C. Van de casteele, Influence of carbonation and  
505 carbonation methods on leaching of metals from mortars, Cement and Concrete Research. 34  
506 (2004) 149–156.

507 [16] M.S. Bin Shafique, J.C. Walton, N. Gutierrez, R.W. Smith, A.J. Tarquin, Influence of  
508 carbonation on leaching of cementitious wastefoms, Journal of Environmental Engineering  
509 (ASCE). 124 (1998) 463–467.

510 [17] P.H.R. Borges, J.O. Costa, N.B. Milestone, C.J. Lynsdale, R.E. Streatfield, Carbonation of  
511 CH and C–S–H in composite cement pastes containing high amounts of BFS, Cement and  
512 Concrete Research. 40 (2013) 284-292.

- 513 [18] J. Han, W. Sun, G. Pan, W. Caihui, Monitoring the evolution of accelerated carbonation of  
514 hardened cement pastes by x-ray computed tomography, *Journal of Materials in Civil Engineering*.  
515 25 (2013) 347-354.
- 516 [19] M. Auroy, S. Poyet, P. Le Bescop, J.M. Torrenti, T. Charpentier, M. Moskura, X. Bourbon,  
517 Impact of carbonation on unsaturated water transport properties of cement-based materials,  
518 *Cement and Concrete Research*. 74 (2015) 44-58.
- 519 [20] L. Greenspan, Humidity fixed points of binary saturated aqueous solutions, *Journal of*  
520 *Research of the National Bureau of Standards – A. Physics and Chemistry*. 81A (1977) 89-96.
- 521 [21] Q. Johnson, R.S. Zhou, Checking and estimating RIR values, *JCPDS-International Centre*  
522 *for Diffraction Data, Advances in X-ray Analysis*. 42 (2000) 287-296.
- 523 [22] ANSI/ANS-16.1–1986 (1986) Measurement of the leachability of solidified low-level  
524 radioactive wastes by a short term test procedure. American Nuclear Society, IL, USA
- 525 [23] T. Ogino, T. Suzuki, K. Sawada, The formation and transformation mechanism of calcium  
526 carbonate in water, *Geochimica and Cosmochimica Acta*. 51(10) (1987) 2757-2767.
- 527 [24] J.L. Wray, F. Daniels, Precipitation of Calcite and Aragonite, *Journal of the American*  
528 *Chemical Society*. 79(7) (1957) 2031-2034.
- 529 [25] M.L.D. Gougar, B.E. Scheetz, D.M. Roy, Ettringite and C-S-H Portland Cement Phases for  
530 Waste Ion Immobilization: A Review. *Waste Management*. 16(4) (1996) 295-303.

- 531 [26] E.T. Stepkowska, J.L. Pérez-Rodríguez, M.J. Sayagués, J.M. Martínez-Blanes, Calcite,  
532 Vaterite and Aragonite forming on cement hydration from liquid and gaseous phase, Journal of  
533 Thermal Analysis and Calorimetry. 73 (2003) 247-269.
- 534 [27] I. Sunagawa, Y. Takahashi, H. Imai, Strontium and aragonite-calcite precipitation, J.  
535 mineralogical and petrological sciences. 102 (2007) 174-181.
- 536 [28] T. Roncal-Herrero, J.D. Rodriguez-Blanco, P. Bots, S. Shaw, L.G. Benning, The Role of  
537 Zn, Sr, Mg and PO<sub>4</sub> in the Interaction of Carbonate-Rich Waters with Sulphate Minerals, revista  
538 de la sociedad española de mineralogía. 15 (2011) 181.
- 539 [29] V.T. Ngala, C.L. Page, Effects of carbonation on pore structure and diffusional properties of  
540 hydrated cement pastes, Cement and Concrete research. 27(7) (1997) 995-1007.
- 541 [30] P. A. Claisse, H. El-Sayad, I.G. Shaaban, Permeability and pore volume of carbonated  
542 concrete, ACI Materials Journal. 96 (3) (1999) 378-382.
- 543 [31] M. Andac & F.P. Glasser, Long-Term leaching mechanisms of Portland cement-stabilized  
544 municipal solid waste fly ash in carbonated water, Cement and Concrete Research. 29 (1999)  
545 179-186.
- 546 [32] J.L. Banner, Application of the trace element and isotope geochemistry of strontium to  
547 studies of carbonate diagenesis, Sedimentology. 42 (1995) 805-824.
- 548 [33] D.J.J. Kinsman, H.D. Holland, The co-precipitation of cations with CaCO<sub>3</sub>-IV. The co-  
549 precipitation of Sr<sup>+2</sup> with aragonite between 16° and 96°C, Geochim. Cosmochim. Acta. 33  
550 (1969) 1-17.

- 551 [34] M. Dietzel, N. Gussone, A. Eisenhauer, Co-precipitation of  $\text{Sr}^{2+}$  and  $\text{Ba}^{2+}$  with aragonite by  
552 membrane diffusion of  $\text{CO}_2$  between 10 and  $50^\circ\text{C}$ , *Chemical geology*. 203 (2004) 139-151.
- 553 [35] Badouix et al. 1999 Toward a validation of the modeling of concrete long term alteration by  
554 natural water attack. *Global proceedings*
- 555 [36] I. Kurashige, M. Hironaga, K. Niwase, Effects of hydrogencarbonate and chloride in ground  
556 water on leaching of cementitious materials. *CONSEC'07 Tours*, (2007) 615-622.
- 557 [37] J. Cowie, F.P. Glasser, The reaction between cement and natural waters containing  
558 dissolved carbon dioxide, *Advanced in Cement Research*. 4 (1992) 119-134.
- 559 [38] A. Dauzères, P. Le Bescop, P. Sardini, C. Cau Dit Coumes, Study of CEMI and low pH  
560 cement pastes leaching in multi-ionic underground water. *CONSEC'10 Mérida*, (2010) 495-503
- 561 [39] Winter J.D., *An introduction to igneous and metamorphic petrology*, 2001, Prentice Hall.
- 562
- 563 Funding: This work was supported by the Israel Atomic Energy Commission (IAEC) and the  
564 French Alternative Energies and Atomic Energy Commission (CEA).
- 565
- 566
- 567
- 568

569 Table 1: Chemical composition of CEM I Val d'Azergues cement (wt%) (Producers data)

SiO <sub>2</sub>	Al <sub>2</sub> O <sub>3</sub>	Fe <sub>2</sub> O <sub>3</sub>	CaO	MgO	K <sub>2</sub> O	Na <sub>2</sub> O	SO <sub>3</sub>	S <sup>-2</sup>	Cl <sup>-</sup>	P <sub>2</sub> O <sub>5</sub>	LOI
20.6	3.6	5.0	64.3	0.7	0.7	0.2	2.7	0.01	0.06	0.4	1.1

570

571

572

573

574

575

576

577

578

579

580

581

582

583

584 Table 2: List of samples (irradiation=IR, climatic chamber=CC, atmospheric=At, inert=In)

Sample experimental condition	Sr doping	Polished before treatment	Treatment	External conditions	leaching	comments
Reference	+	-	-	-	+	
Climatic chamber atmospheric	+	+	CC	At	+	
Climatic chamber inert	+	+	CC	In	+	
Irradiated atmospheric	+	-	IR	At	+	
Irradiated inert (blank)	-	-	IR	In	+	Natural Sr concentration
Irradiated inert (unleached)	+	-	IR	In	-	

585

586

587

588

589

590

591

592 Table 3: Crystallographic data for the XRD RIR analysis (from ICSD using POWD-12++)

mineral	$2\theta$	RIR	peak fraction
Calcite	29.3	3.2	1
Aragonite	26.1	1.13	1
Vaterite	26.9	1.14	1
Portlandite	17.9	3.46	0.74

593

594

595

596

597

598

599

600

601

602

603

604 Table 4: List of analyzed isotopes, their average limit of detection and average analytical error  
 605 percent for the different spot sizes

606

Spot size	10 $\mu\text{m}$		50 $\mu\text{m}$		100 $\mu\text{m}$	
	LOD ( $\mu\text{g/g}$ )	% error	LOD ( $\mu\text{g/g}$ )	% error	LOD ( $\mu\text{g/g}$ )	% error
$^{25}\text{Mg}$	76	2.4	2.7	0.6	0.9	0.2
$^{29}\text{Si}$	3083	1.7	111	0.4	29	0.1
$^{42}\text{Ca}$	3696	1.0	94	0.1	26	0.1
$^{43}\text{Ca}$	1653	1.5	68	0.3	24	0.1
$^{88}\text{Sr}$	1.4	0.8	0.1	0.2	0.02	0.1
$^{137}\text{Ba}$	7.3	8.1	0.4	1.9	0.1	0.8

607

608

609

610

611

612

613

614 **Figure captions:**

615 Figure 1: The sampling spot size and relative concentration of Ca and Mg as a function of the  
616 distance from the sample surface in a leached sample.  $C$  = the concentration at a specific distance,  
617  $C_0$  = the concentration at the undisturbed inner sample volume.

618 Figure 2: EPMA BSE image of sample surface irradiated under inert atmosphere.

619 Figure 3: Relative concentration of Ca, Ba and Sr as obtained by LA-ICPMS along a cross section in a  
620 sample irradiated under inert conditions

621 Figure 4: XRD profiles of samples treated under atmospheric conditions. (a) sample treated in  
622 climatic chamber, (b) sample irradiated

623 Figure 5: Cracking on sample exposed to atmospheric conditions in the climatic chamber

624 Figure 6: Sr Cumulative fraction as a function of square root of leaching time. The error bars  
625 represent the average deviation of duplicate samples.

626 Figure 7: Ca Cumulative fraction as a function of square root of leaching time. The error bars  
627 represent the average deviation of duplicate samples

628 Figure 8: Sr Cumulative fraction for samples irradiated under inert conditions doped and un-doped  
629 with Sr as a function of square root of leaching time.

630 Figure 9: EPMA BSE image of the untreated reference leached sample

631 Figure 10: the Sr, Ca and Ba concentration variation along a cross section in the  
632 untreated reference leached sample

633 Figure 11: XRD profile of the untreated reference leached sample

634 Figure 12: EPMA BSC image of leached sample after treatment in the climatic chamber under  
635 inert atmosphere.

636 Figure 13: LA-ICP-MS Ca, Ba and Sr concentration variation along a cross section in the two  
637 leached samples after treatment under inert atmosphere.(a) climatic chamber (b) irradiated

638 Figure 14: Phase distribution along a cross section in the leached samples after treatment under  
639 inert atmosphere (a) in the climatic chamber (b) irradiated

640 Figure 15: EPMA BSE images of leached sample treated in the climatic chamber under  
641 atmospheric conditions. Zoom into the near edge area (surface on the top).

642 Figure 16: The Ca, Ba and Sr concentrations along a cross section in leached samples after  
643 treatment under atmospheric conditions; (a) in the climatic chamber (b) irradiated

644 Figure 17: Phase distribution along a cross section in the leached samples after treatment under  
645 atmospheric conditions (a) in the climatic chamber (b) irradiated

646

647

648

649

650

651

652

653

654

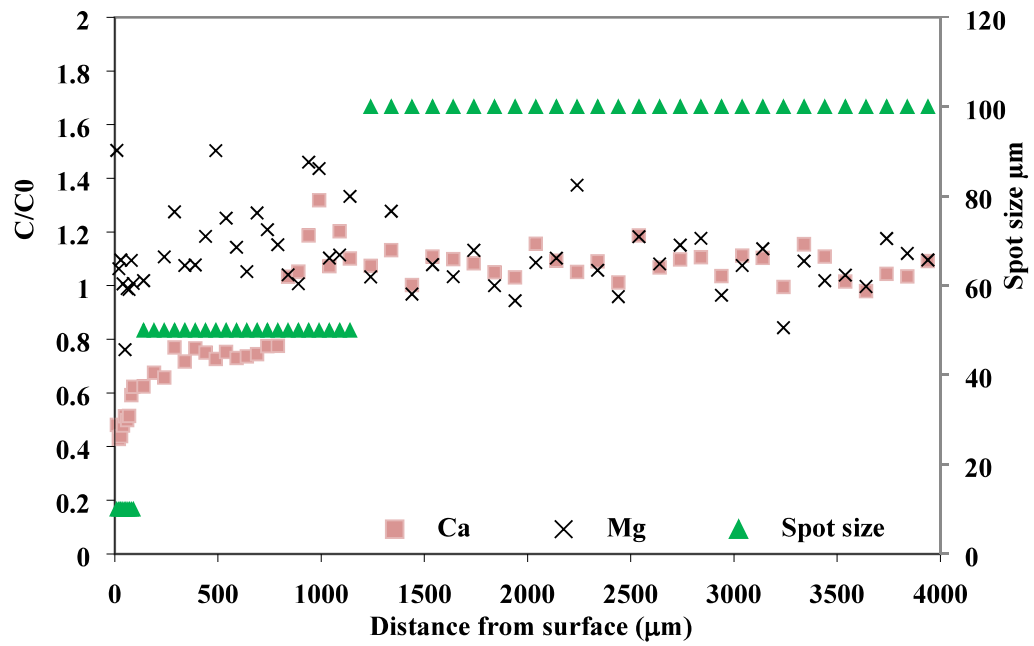


Figure 1: The sampling spot size and relative concentration of Ca and Mg as a function of the distance from the sample surface in a leached sample.  $C$  = the concentration at a specific distance,  $C_0$  = the concentration at the undisturbed inner sample volume.

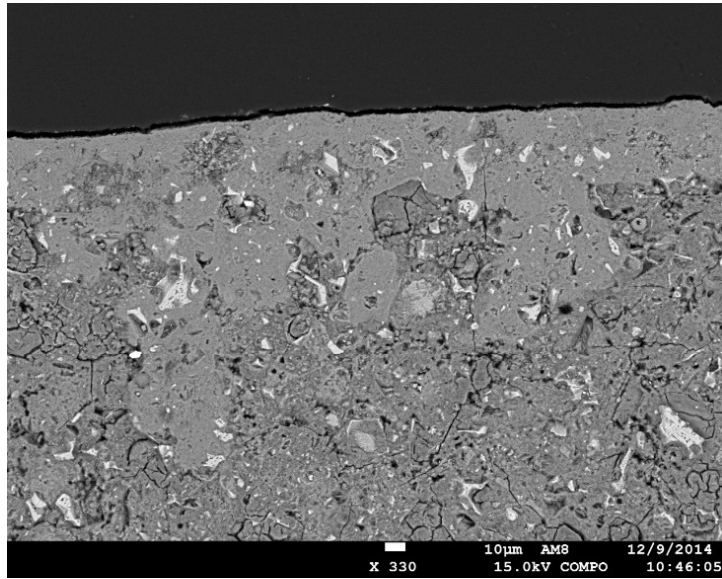


Figure 2: EPMA BSE image of sample surface irradiated under inert atmosphere.

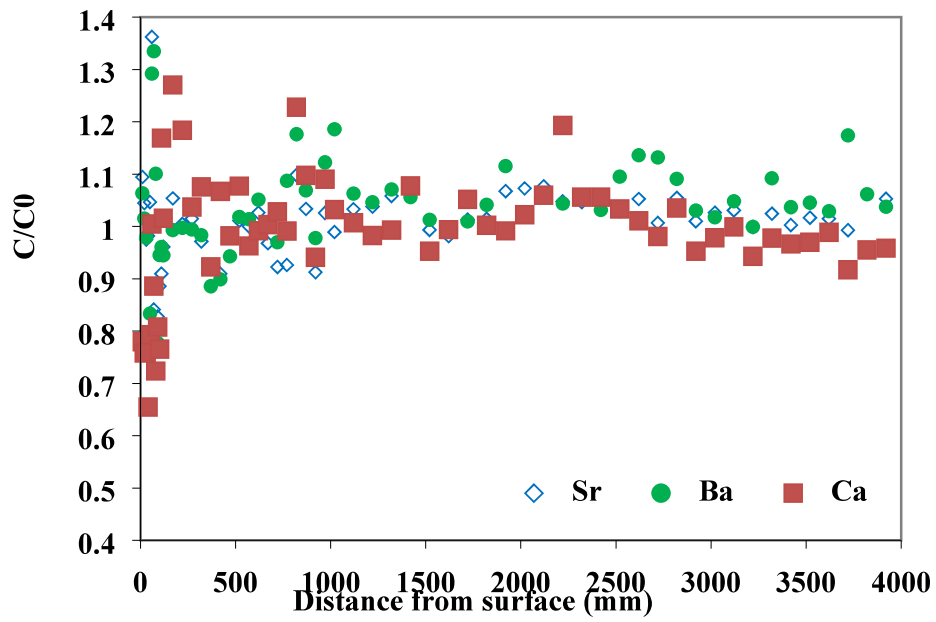


Figure 3: Relative concentration of Ca, Ba and Sr as obtained by LA-ICPMS along a cross section in a sample irradiated under inert conditions

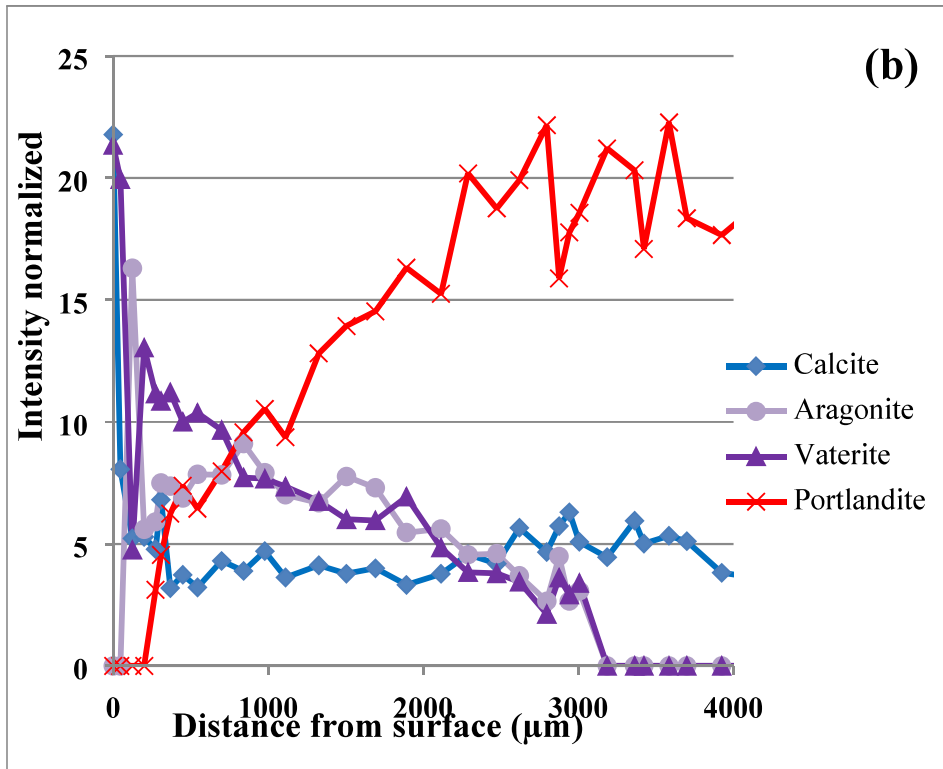
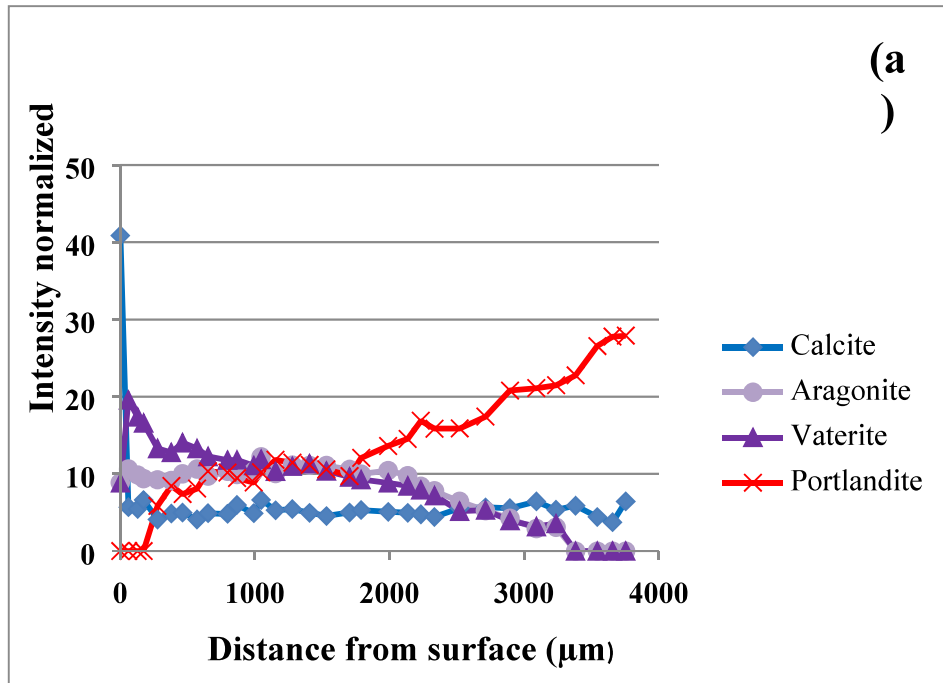


Figure 4: XRD profiles of samples treated under atmospheric conditions. (a) sample treated in climatic chamber, (b) sample irradiated

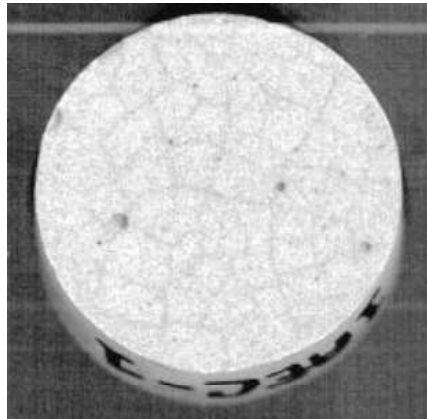


Figure 5: Cracking on sample exposed to atmospheric conditions in the climatic chamber

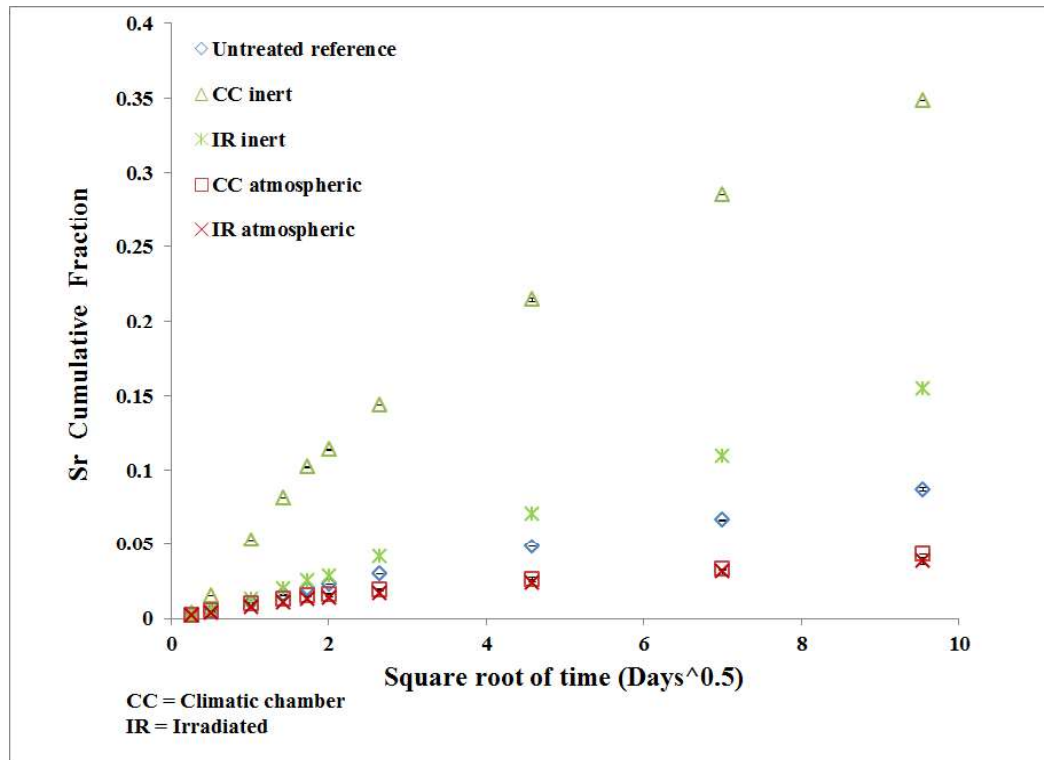


Figure 6: Sr Cumulative fraction as a function of square root of leaching time. The error bars represent the average deviation of duplicate samples.

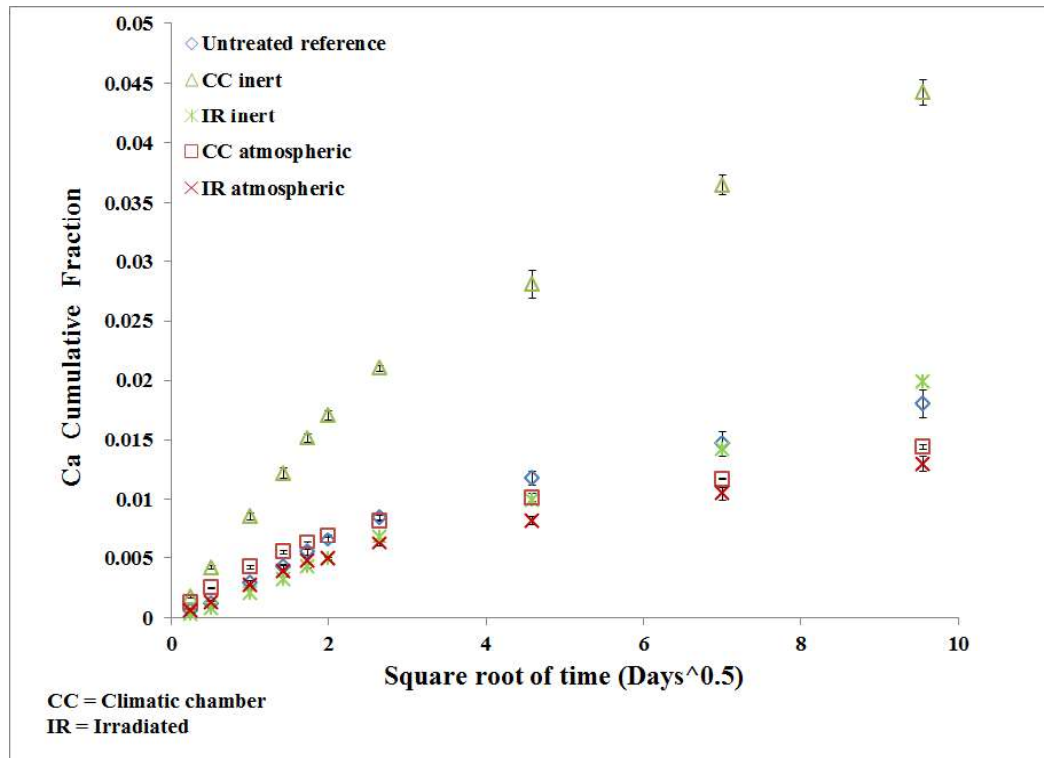


Figure 7: Ca Cumulative fraction as a function of square root of leaching time. The error bars represent the average deviation of duplicate samples

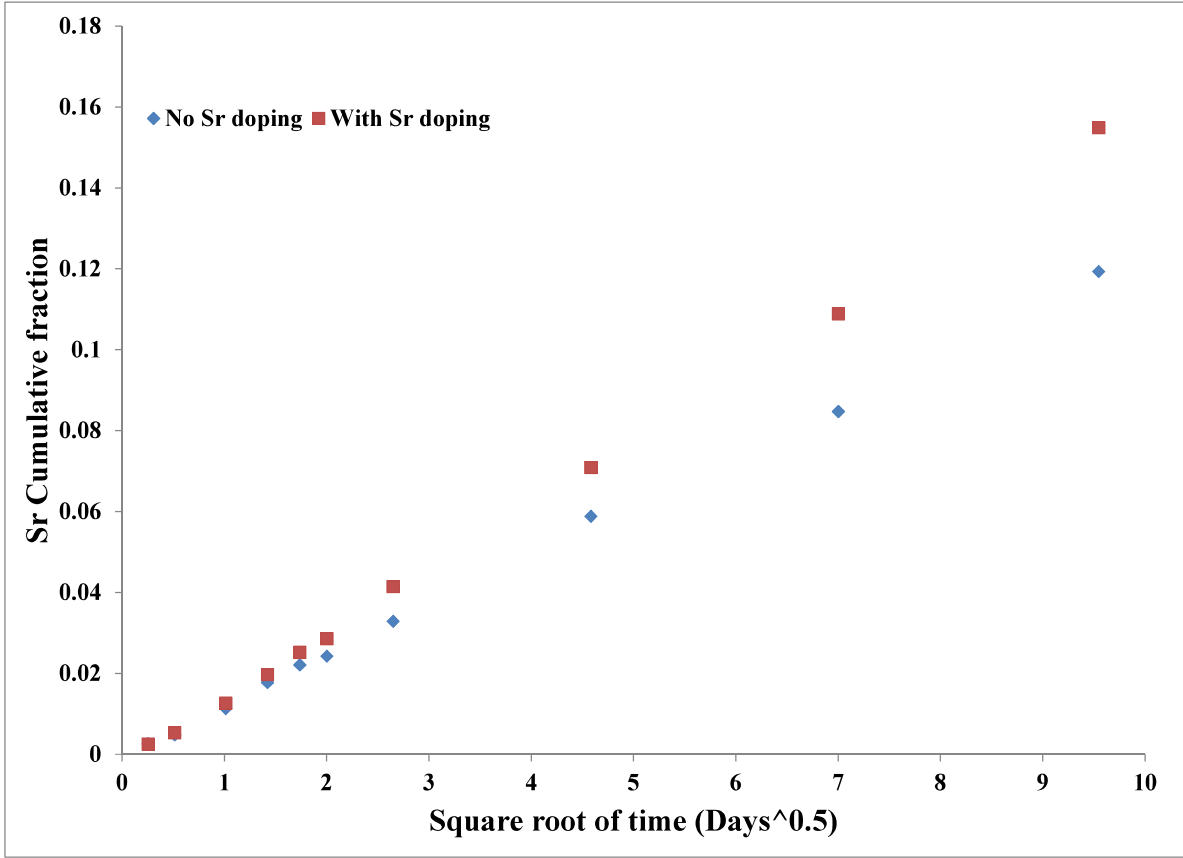


Figure 8: Sr Cumulative fraction for samples irradiated under inert conditions doped and un-doped with Sr as a function of square root of leaching time.

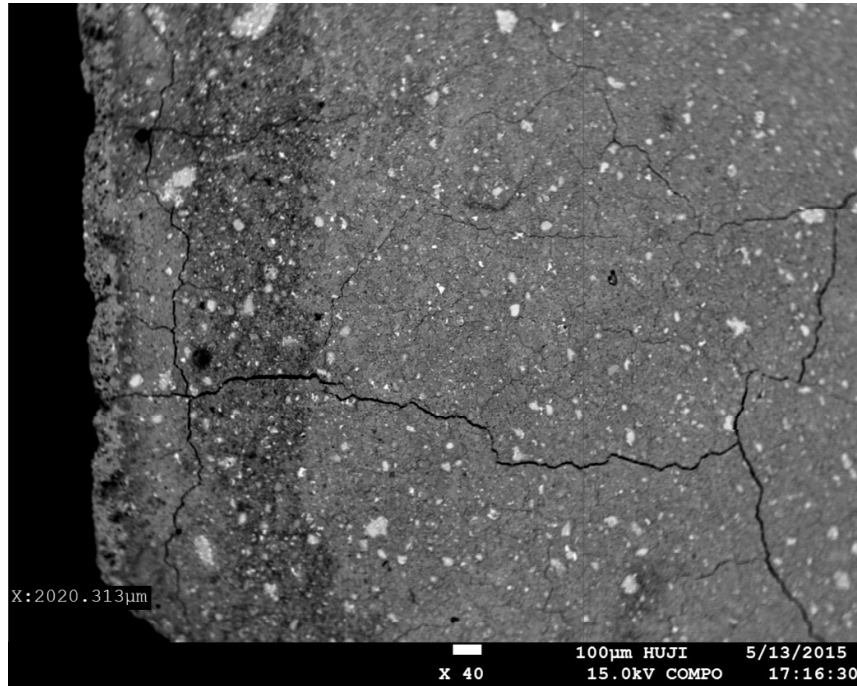


Figure 9: EPMA BSE image of the untreated reference leached sample

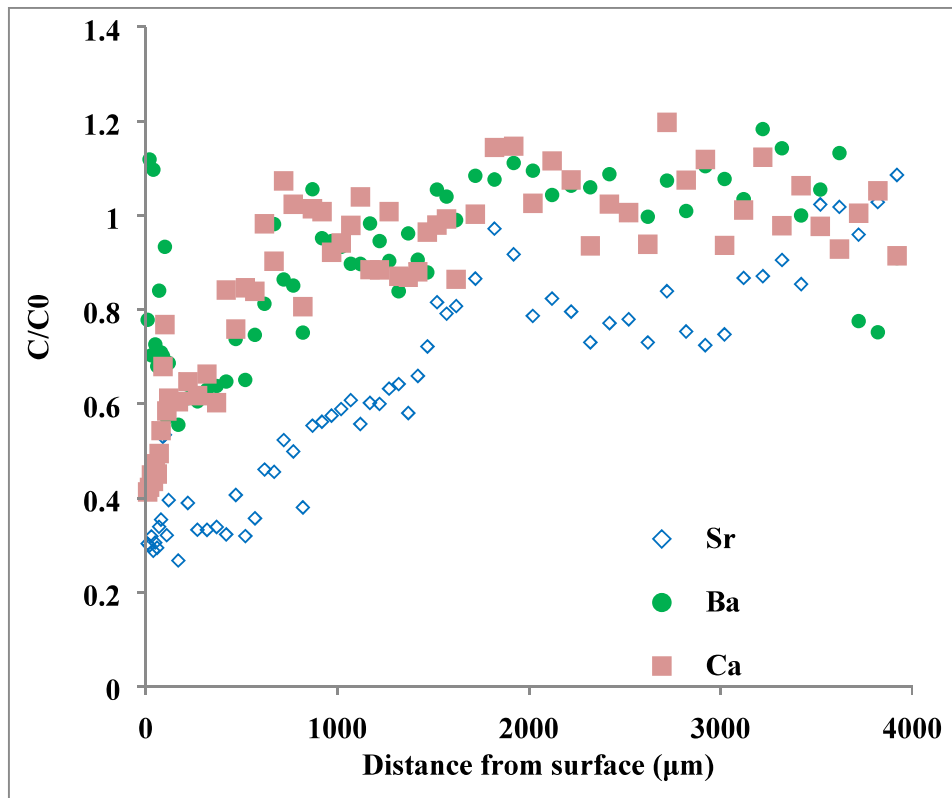


Figure 10: the Sr, Ca and Ba concentration variation along a cross section in the untreated reference leached sample

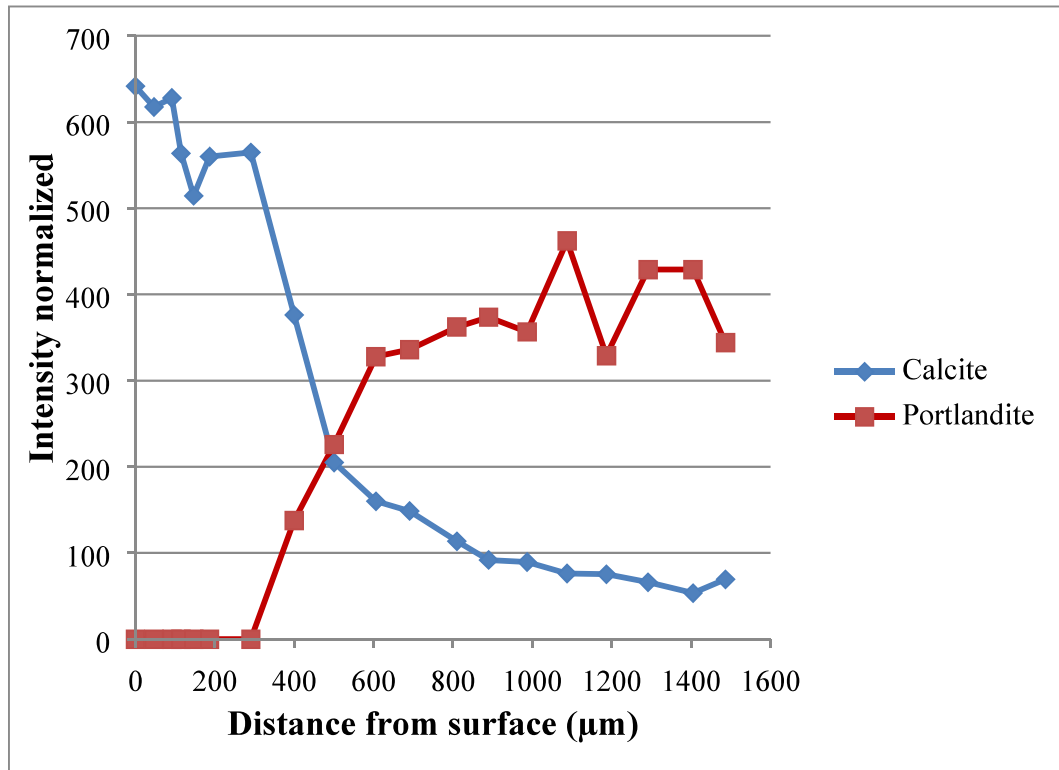


Figure 11: XRD profile of the untreated reference leached sample

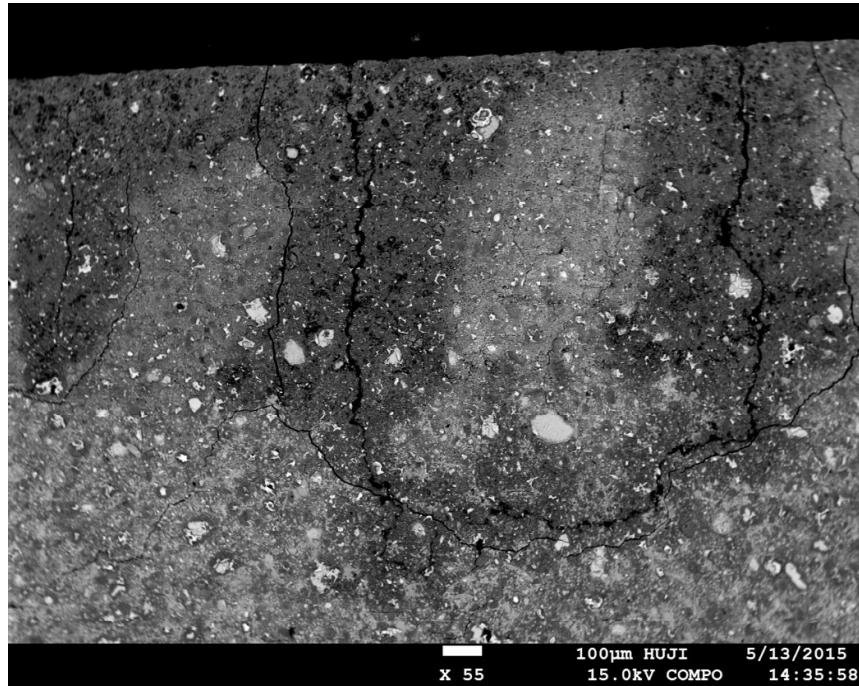


Figure 12: EPMA BSC image of leached sample after treatment in the climatic chamber under inert atmosphere.

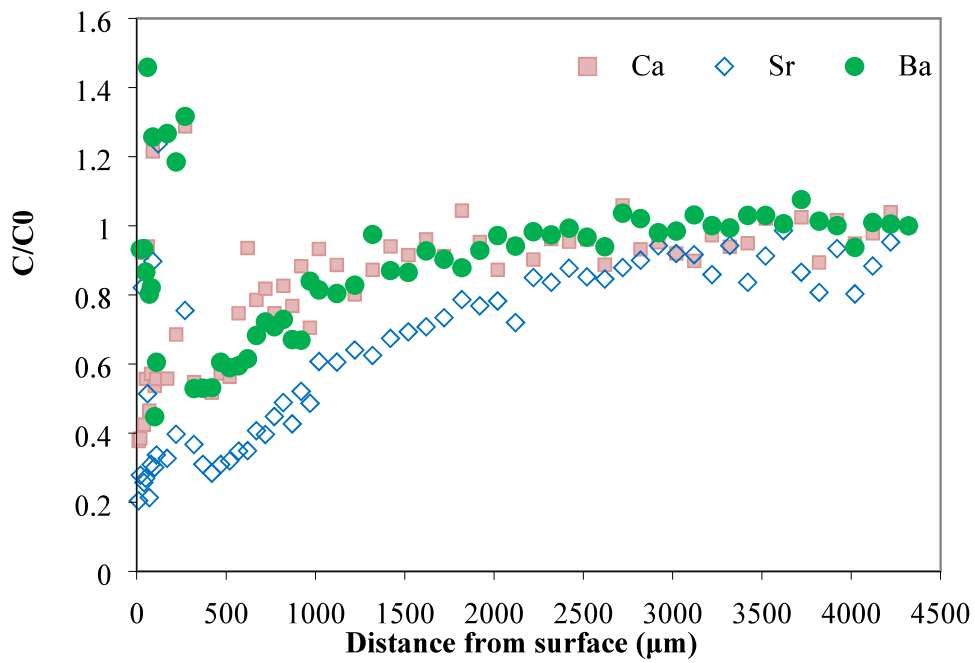
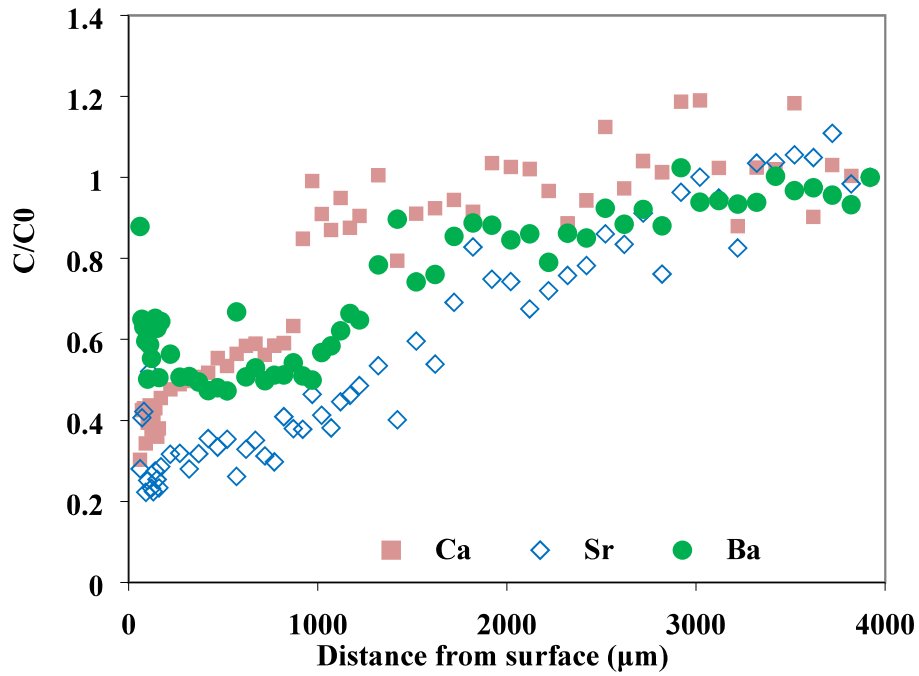


Figure 13: LA-ICP-MS Ca, Ba and Sr concentration variation along a cross section in the two leached samples after treatment under inert atmosphere:(a) climatic chamber (b) irradiated

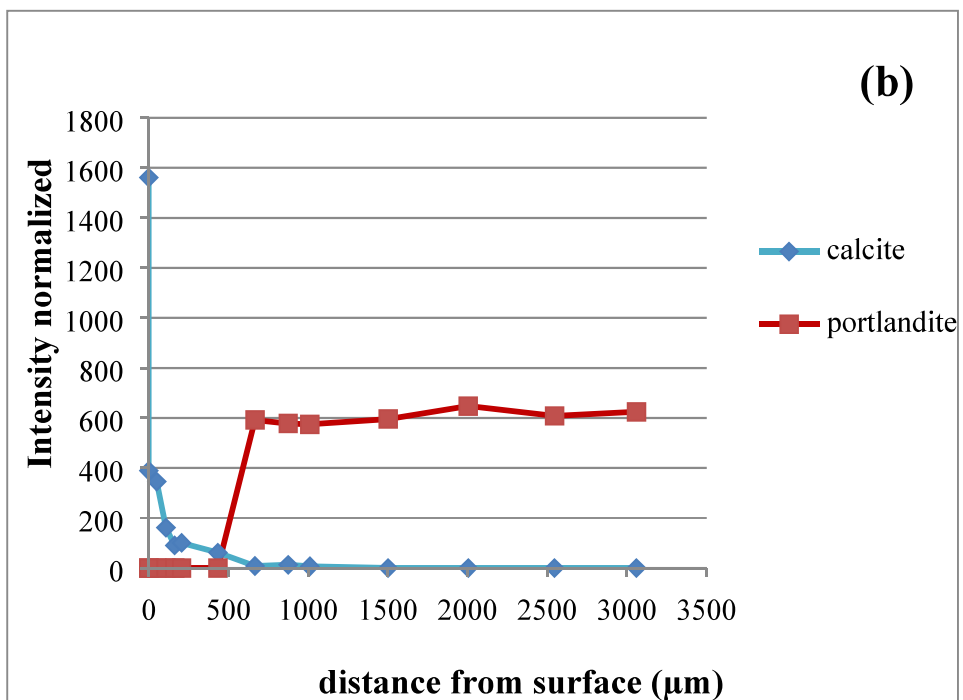
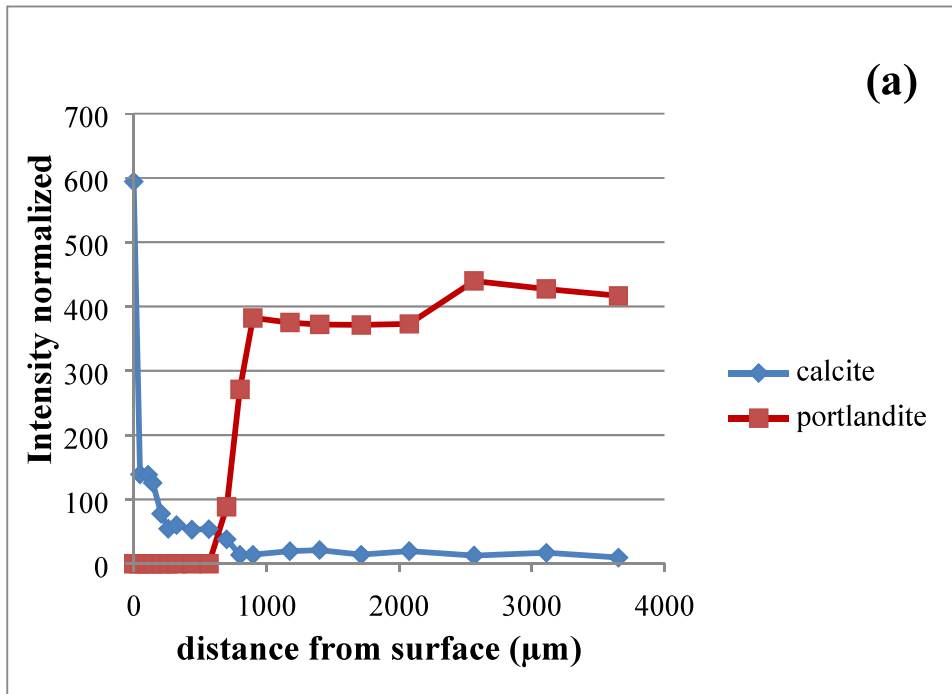


Figure 14: Phase distribution along a cross section in the leached samples after treatment under inert atmosphere (a) in the climatic chamber (b) irradiated

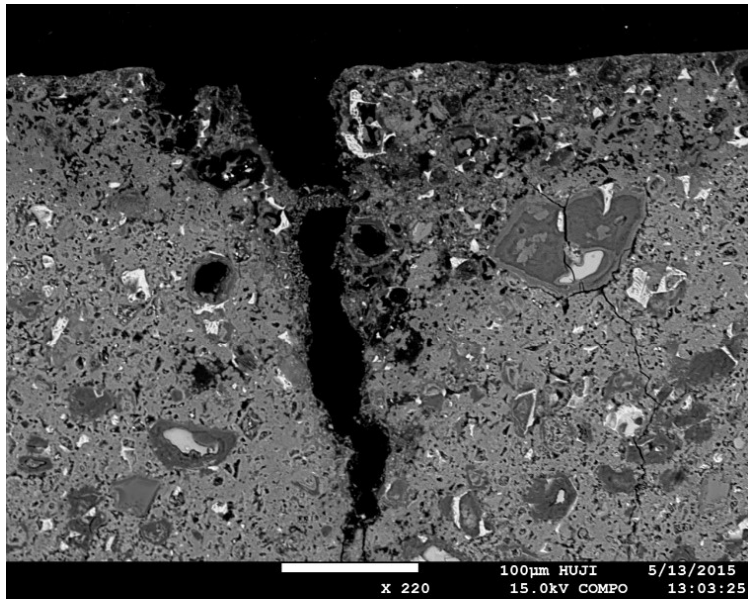


Figure 15: EPMA BSE images of leached sample treated in the climatic chamber under atmospheric conditions. Zoom into the near edge area (surface on the top).

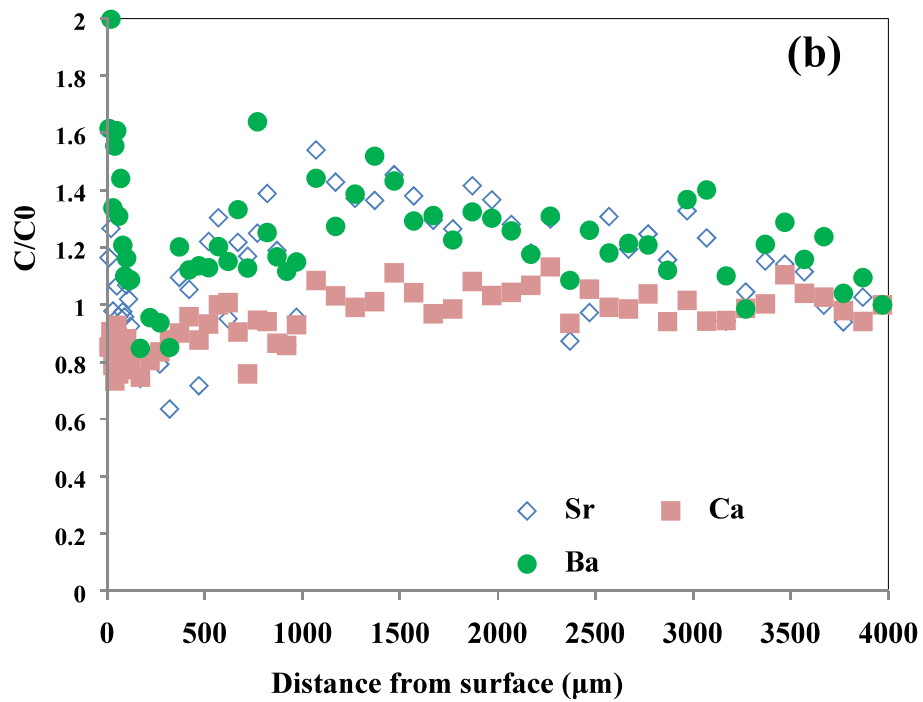
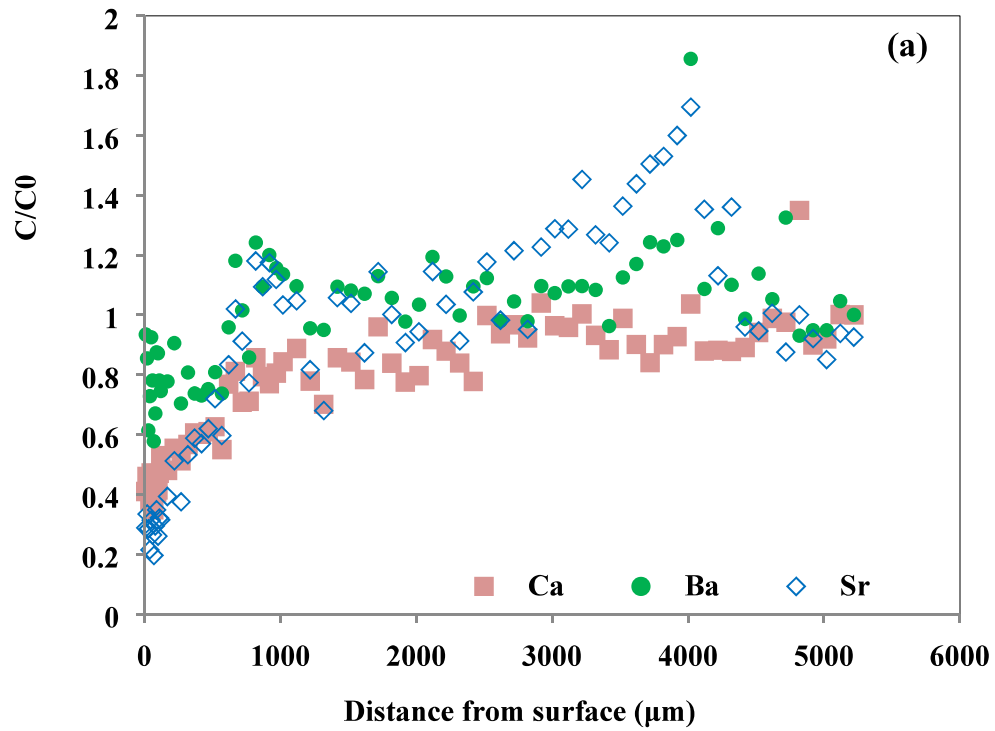


Figure 16: The Ca, Ba and Sr concentrations along a cross section in leached samples after treatment under atmospheric conditions; (a) in the climatic chamber (b) irradiated

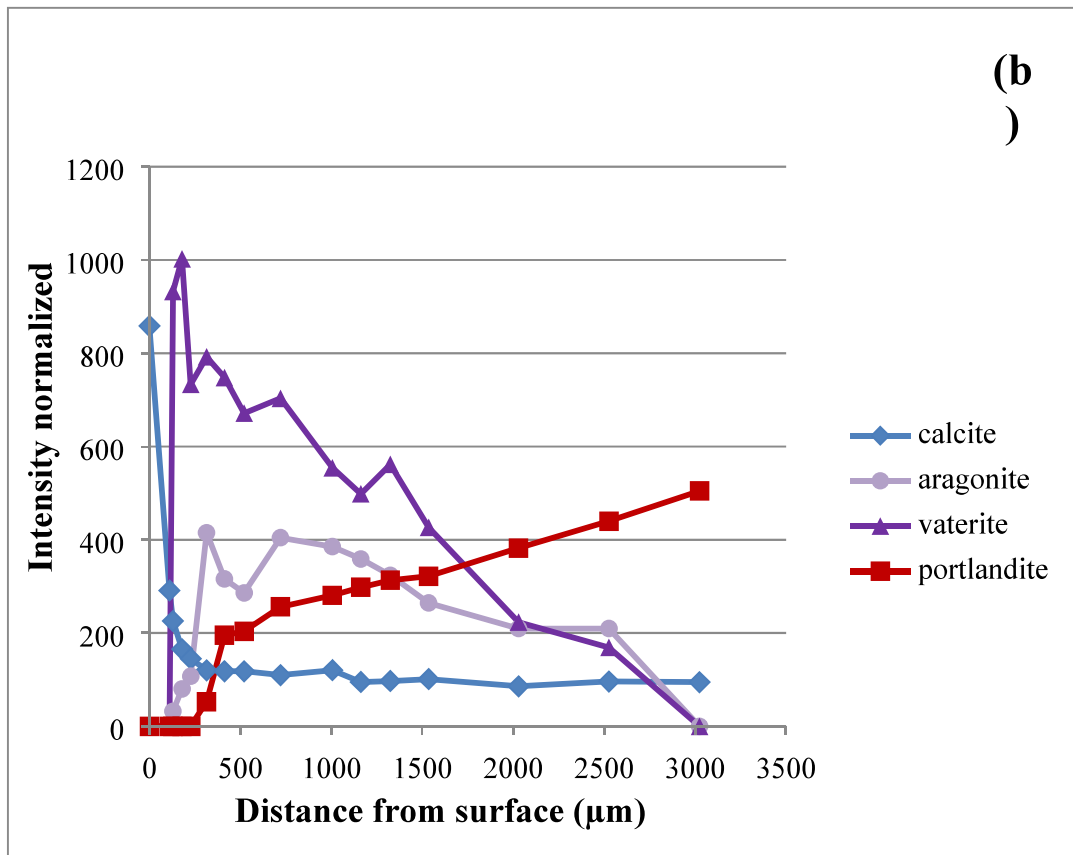
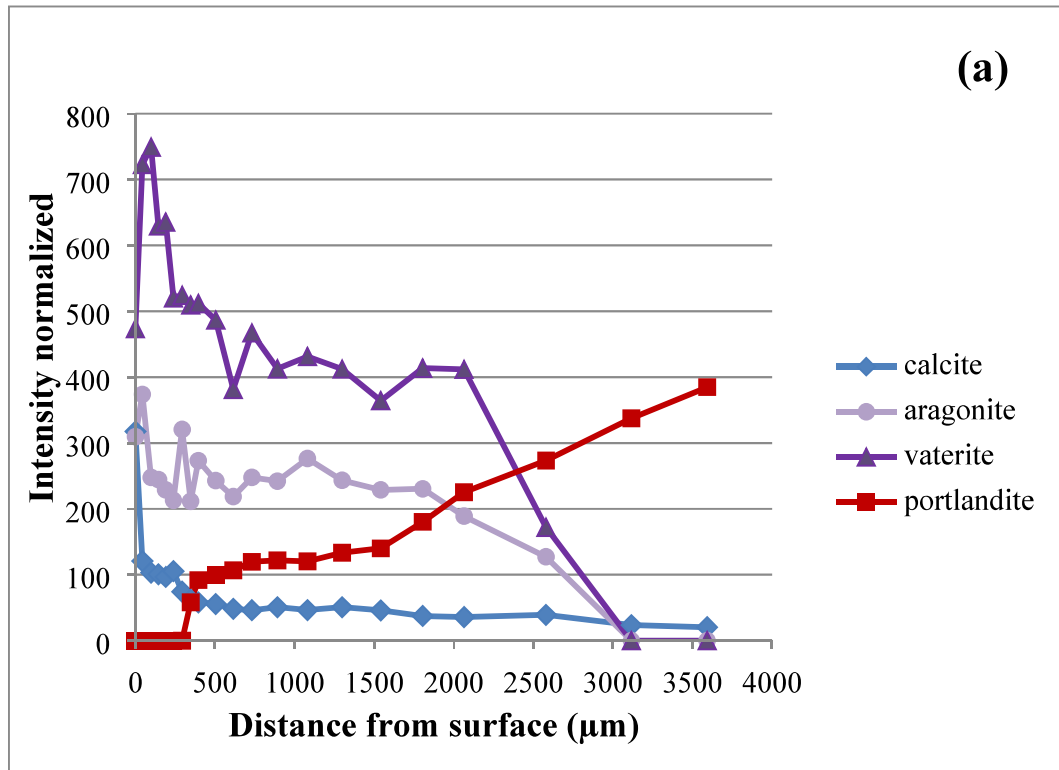


Figure 17: Phase distribution along a cross section in the leached samples after treatment under atmospheric conditions (a) in the climatic chamber (b) irradiated